Electrophysiology

Electrophysiological methods were performed as described previously[27,28]. In brief, animals were immobilized with a cyanoacrylic glue and a lateral incision was made to expose the ventral nerve cord and body wall muscles. Muscle recordings were made in the whole-cell voltage-clamp configuration (holding potential −60 mV) at room temperature (19 °C) with an EPC-10-2 patch-clamp amplifier (HEKA, Lambrecht, Germany) and digitized at 2.9 kHz by means of an ITC-16 interface (Instrutech, Great Neck, New York, USA). Data were acquired by Pulse software (HEKA). The bath solution contained 150 mM NaCl, 5 mM KCl, 5 mM $CaCl_2$, 1 mM $MgCl_2$, 10 mM glucose and 15 mM HEPES pH 7.35; ~330 mOsm. The pipette solution contained 120 mM KCl, 20 mM KOH, 4 mM $MgCl_2$, 5 mM (*N*-tris(hydroxymethyl)methyl-2-aminoethane-sulphonic acid), 0.25 mM $CaCl_2$, 4 mM NaATP, 36 mM sucrose, 5 mM EGTA pH 7.2; ~315 mOsm. Subsequent analysis and graphing were performed using Pulsefit (HEKA), Mini Analysis (Synaptosoft) and Igor Pro (Wavemetrics, Lake Oswego, Oregon, USA).

Immunoprecipitation and western blotting

snf-6 and *stn-1* cDNAs, tagged with Flag and haemagglutinin (HA) epitopes, respectively, were subcloned to a mammalian expression vector. An equal amount of each construct was transfected into COS-7 cells with FUGENE 6 (Roche). The transfected cells were lysed with lysis buffer (50 mM Tris-HCl pH 7.4, 1% Nonidet P40, 0.25% sodium deoxycholate, 10% glycerol, 150 mM NaCl and a mixture of protease inhibitors) and the resulting lysates were used for immunoprecipitation with anti-Flag (Roche) or anti-HA (Sigma) antibodies. Immune complexes were resolved by 8% SDS–polyacrylamide-gel electrophoresis and then transferred to poly(vinylidene difluoride) membrane. Each blotted membrane was cut into two different parts for western blotting with anti-HA and anti-FLAG antibodies.

Staining and microscopy

For actin fibre staining, 4-day-old adult animals grown at 15 °C were fixed with 4% paraformaldehyde for 16 h and treated with collagenase (2,000 U ml^{-1})[29], then stained with Alexa Fluor 488 phalloidin (Molecular Probes). Animals were scored as having degenerated muscles if we observed disorganized muscle fibres in at least two muscle quadrants (40 cells). Aldicarb treatment was performed on plates from the L1 larval stage at a concentration (10 μM) that does not cause complete paralysis.

To observe fluorescence from transgenic animals expressing GFP, animals were mounted on a 4% agar pad containing sodium azide. In the cases that required quantification of the levels of fluorescence in different genetic backgrounds, a SPOT CCD camera was used to capture images for a fixed time interval, and pixel intensity at the NMJs was determined for each sample with NIH image 1.63. At least 30 animals were randomly chosen for quantification of fluorescence levels in each line. The percentage of animals showing detectable expression did not vary significantly between lines (data not shown).

Received 11 May; accepted 2 July 2004; doi:10.1038/nature02798.

1. Durbeej, M. & Campbell, K. P. Muscular dystrophies involving the dystrophin–glycoprotein complex: an overview of current mouse models. *Curr. Opin. Genet. Dev.* **12,** 349–361 (2002).
2. McArdle, A., Edwards, R. H. & Jackson, M. J. Time course of changes in plasma membrane permeability in the dystrophin-deficient *mdx* mouse. *Muscle Nerve* **17,** 1378–1384 (1994).
3. Grady, R. M. *et al.* Maturation and maintenance of the neuromuscular synapse: genetic evidence for roles of the dystrophin–glycoprotein complex. *Neuron* **25,** 279–293 (2000).
4. Burton, E. A. & Davies, K. E. in *Pathogenesis of Neurodegenerative Disorders* (ed. Mattson, M. P.) 239–284 (Humana Press, Totowa, New Jersey, 2000).
5. Bessou, C., Giugia, J. B., Franks, C. J., Holden-Dye, L. & Segalat, L. Mutations in the *Caenorhabditis elegans* dystrophin-like gene *dys-1* lead to hyperactivity and suggest a link with cholinergic transmission. *Neurogenetics* **2,** 61–72 (1998).
6. Gieseler, K., Bessou, C. & Segalat, L. Dystrobrevin- and dystrophin-like mutants display similar phenotypes in the nematode *Caenorhabditis elegans*. *Neurogenetics* **2,** 87–90 (1999).
7. Grisoni, K., Martin, E., Gieseler, K., Mariol, M. C. & Segalat, L. Genetic evidence for a dystrophin–glycoprotein complex (DGC) in *Caenorhabditis elegans*. *Gene* **294,** 77–86 (2002).
8. Davies, A. G. *et al.* A central role of the BK Potassium channel in behavioral responses to ethanol in *C. elegans*. *Cell* **115,** 655–666 (2003).
9. Shioi, G. *et al.* Mutations affecting nerve attachment of *Caenorhabditis elegans*. *Genetics* **157,** 1611–1622 (2001).
10. Giugia, J., Gieseler, K., Arpagaus, M. & Segalat, L. Mutations in the dystrophin-like *dys-1* gene of *Caenorhabditis elegans* result in reduced acetylcholinesterase activity. *FEBS Lett.* **463,** 270–272 (1999).
11. Gieseler, K. *et al.* Molecular, genetic and physiological characterisation of dystrobrevin-like (*dyb-1*) mutants of *Caenorhabditis elegans*. *J. Mol. Biol.* **307,** 107–117 (2001).
12. Froehner, S. C., Adams, M. E., Peters, M. F. & Gee, S. H. Syntrophins: modular adapter proteins at the neuromuscular junction and the sarcolemma. *Soc. Gen. Physiol. Ser.* **52,** 197–207 (1997).
13. Gieseler, K., Abdel-Dayem, M. & Segalat, L. *In vitro* interactions of *Caenorhabditis elegans* dystrophin with dystrobrevin and syntrophin. *FEBS Lett.* **461,** 59–62 (1999).
14. Megeney, L. A., Kablar, B., Garrett, K., Anderson, J. E. & Rudnicki, M. A. MyoD is required for myogenic stem cell function in adult skeletal muscle. *Genes Dev.* **10,** 1173–1183 (1996).
15. Gieseler, K., Grisoni, K. & Segalat, L. Genetic suppression of phenotypes arising from mutations in dystrophin-related genes in *Caenorhabditis elegans*. *Curr. Biol.* **10,** 1092–1097 (2000).
16. Mariol, M. C. & Segalat, L. Muscular degeneration in the absence of dystrophin is a calcium-dependent process. *Curr. Biol.* **11,** 1691–1694 (2001).
17. Potter, L. T. Synthesis, storage and release of [^{14}C]acetylcholine in isolated rat diaphragm muscles. *J. Physiol. (Lond.)* **206,** 145–166 (1970).
18. Saelens, J. K. & Stoll, W. R. Radiochemical determination of choline and acetylcholine flux from isolated tissue. *J. Pharmacol. Exp. Ther.* **147,** 336–342 (1965).
19. Salpeter, M. M., Kasprzak, H., Feng, H. & Fertuck, H. Endplates after esterase inactivation *in vivo*: correlation between esterase concentration, functional response and fine structure. *J. Neurocytol.* **8,** 95–115 (1979).
20. Leonard, J. P. & Salpeter, M. M. Agonist-induced myopathy at the neuromuscular junction is mediated by calcium. *J. Cell Biol.* **82,** 811–819 (1979).
21. Jackson, M. J., Jones, D. A. & Edwards, R. H. Measurements of calcium and other elements in muscle biopsy samples from patients with Duchenne muscular dystrophy. *Clin. Chim. Acta* **147,** 215–221 (1985).
22. Kramarcy, N. R. & Sealock, R. Syntrophin isoforms at the neuromuscular junction: developmental time course and differential localization. *Mol. Cell. Neurosci.* **15,** 262–274 (2000).
23. Webster, C., Silberstein, L., Hays, A. P. & Blau, H. M. Fast muscle fibers are preferentially affected in Duchenne muscular dystrophy. *Cell* **52,** 503–513 (1988).
24. Karpati, G., Carpenter, S. & Prescott, S. Small-caliber skeletal muscle fibers do not suffer necrosis in *mdx* mouse dystrophy. *Muscle Nerve* **11,** 795–803 (1988).
25. Brenner, S. The genetics of *Caenorhabditis elegans*. *Genetics* **77,** 71–94 (1974).
26. Miyabayashi, T., Palfreyman, M. T., Sluder, A. E., Slack, F. & Sengupta, P. Expression and function of members of a divergent nuclear receptor family in *Caenorhabditis elegans*. *Dev. Biol.* **215,** 314–331 (1999).
27. Richmond, J. E. & Jorgensen, E. M. One GABA and two acetylcholine receptors function at the *C. elegans* neuromuscular junction. *Nature Neurosci.* **2,** 791–797 (1999).
28. Richmond, J. E., Davis, W. S. & Jorgensen, E. M. UNC-13 is required for synaptic vesicle fusion in *C. elegans*. *Nature Neurosci.* **2,** 959–964 (1999).
29. Waterston, R. H., Hirsh, D. & Lane, T. R. Dominant mutations affecting muscle structure in *Caenorhabditis elegans* that map near the actin gene cluster. *J. Mol. Biol.* **180,** 473–496 (1984).

Supplementary Information accompanies the paper on **www.nature.com/nature**.

Acknowledgements We thank J. S. Kim, C. Yu and R. Ho for technical help, J. Rand and C. Bargmann for personal communication and helpful discussions, and all members of the McIntire laboratory for discussions and comments on the manuscript. Some strains were provided by the National Bioresource Project (Japan), the *C. elegans* Gene Knockout Consortium and the *Caenorhabditis* Genetics Center. This work was supported by funds provided by the State of California for medical research on alcohol and substance abuse through the University of California, San Francisco, by a grant to S.L.M. from the Department of the Army, by a grant to J.E.R. from NIH and by a development grant to H.K. from the Muscular Dystrophy Association.

Competing interests statement The authors declare that they have no competing financial interests.

Correspondence and requests for materials should be addressed to S.L.M. (e-mail: slm@itsa.ucsf.edu).

Coupling of agonist binding to channel gating in an ACh-binding protein linked to an ion channel

Cecilia Bouzat[1], Fernanda Gumilar[1], Guillermo Spitzmaul[1], Hai-Long Wang[2], Diego Rayes[1], Scott B. Hansen[3], Palmer Taylor[3] & Steven M. Sine[2]

[1]*Instituto de Investigaciones Bioquimicas, UNS-CONICET, Bahia Blanca 8000, Argentina*
[2]*Receptor Biology Laboratory, Department of Physiology and Biomedical Engineering, Mayo Clinic College of Medicine, Rochester, Minnesota 55905, USA*
[3]*Department of Pharmacology, University of California, San Diego, La Jolla, California 92093-0636, USA*

Neurotransmitter receptors from the Cys-loop superfamily couple the binding of agonist to the opening of an intrinsic ion pore in the final step in rapid synaptic transmission. Although atomic resolution structural data have recently emerged for individual binding[1] and pore domains[2], how they are linked into a functional unit remains unknown. Here we identify structural requirements for functionally coupling the two domains by combining acetylcholine (ACh)-binding protein, whose structure was determined at atomic resolution[1], with the pore domain from the serotonin type-3A (5-HT_{3A}) receptor. Only when amino-acid sequences of three loops in ACh-binding protein are changed to their 5-HT_{3A} counterparts does ACh bind with low affinity characteristic of activatable receptors, and trigger opening of the ion pore. Thus functional coupling requires structural compatibility at the interface of the binding

and pore domains. Structural modelling reveals a network of interacting loops between binding and pore domains that mediates this allosteric coupling process.

Pentameric ligand-gated ion channels mediate rapid synaptic transmission throughout the nervous system, and include receptors activated by ACh, γ-aminobutyric acid, glycine and 5-HT (refs 3–5). Their vital role in converting chemical recognition into an electrical impulse makes these receptors prime loci for learning, memory and disease processes, as well as targets for clinically relevant drugs. Activation of synaptic receptors comprises three elementary steps: agonist recognition, coupling to the ion pore and opening of the pore. Each step has a physical counterpart, and recent X-ray crystallographic and electron microscopic data cast considerable light on the atomic structures of the binding[1] and pore counterparts[2]. However, the structural basis for functionally coupling binding and pore domains remains a topic of intense investigation[2,6,7].

To investigate the structural basis for functionally coupling binding and pore domains, we generated a chimaeric receptor composed of the ACh binding domain from acetylcholine binding protein (AChBP) and the pore domain from the 5-HT_{3A} receptor (Fig. 1a). AChBP was chosen because its atomic structure is known[1], and it presumably evolved without the constraint of functional coupling to an ionic pore, whereas the 5-HT_{3A} pore enables expression of homo-pentameric receptors in mammalian cells[8,9]. After transfection of the chimaeric complementary DNA into Bosc 23 cells, robust quantities of the receptor chimaera are expressed on the surface of the cells, as measured by α-bungarotoxin binding, and ACh binds to the chimaera with micro-molar affinity (Table 1). However, reliable ACh-induced currents could not be detected using the patch clamp. We therefore reasoned that although binding and pore domains were correctly folded, enabling expression on the cell surface, the interface between the two domains was not compatible, preventing inter-domain coupling.

From the known atomic coordinates of AChBP (ref. 1) and the pore domain of the *Torpedo* acetylcholine receptor[2], we generated a homology model of our chimaeric receptor (Fig. 1b, c). Each subunit contains an AChBP module composed of ten β-strands and interconnecting loops, and a pore domain containing four α-helices. The model shows three of the interconnecting loops from the binding domain project into or near the pore domain, and the loop connecting M2 and M3 helices of the pore domain projects into the binding domain. We hypothesized that interplay between these four loops is crucial for functional coupling.

To test this hypothesis, we mutated residues in AChBP to their 5-HT_{3A} counterparts in the three loops that face the pore, thus generating two new chimaeras designated C3 and C3L (Table 1 and Fig. 1a); these chimaeras are identical except that C3L contains three additional residues of the 5-HT_{3A} sequence substituted in the β8–β9 loop. Both chimaeras express robust quantities of cell surface receptors in Bosc 23 cells, and show a 20- to 40-fold increase in apparent dissociation constant (K_d) for ACh binding (Table 1). Expression amounts and apparent K_d for ACh are distinct from those of the AChBP/5-HT_{3A} chimaera, but are similar to those of a

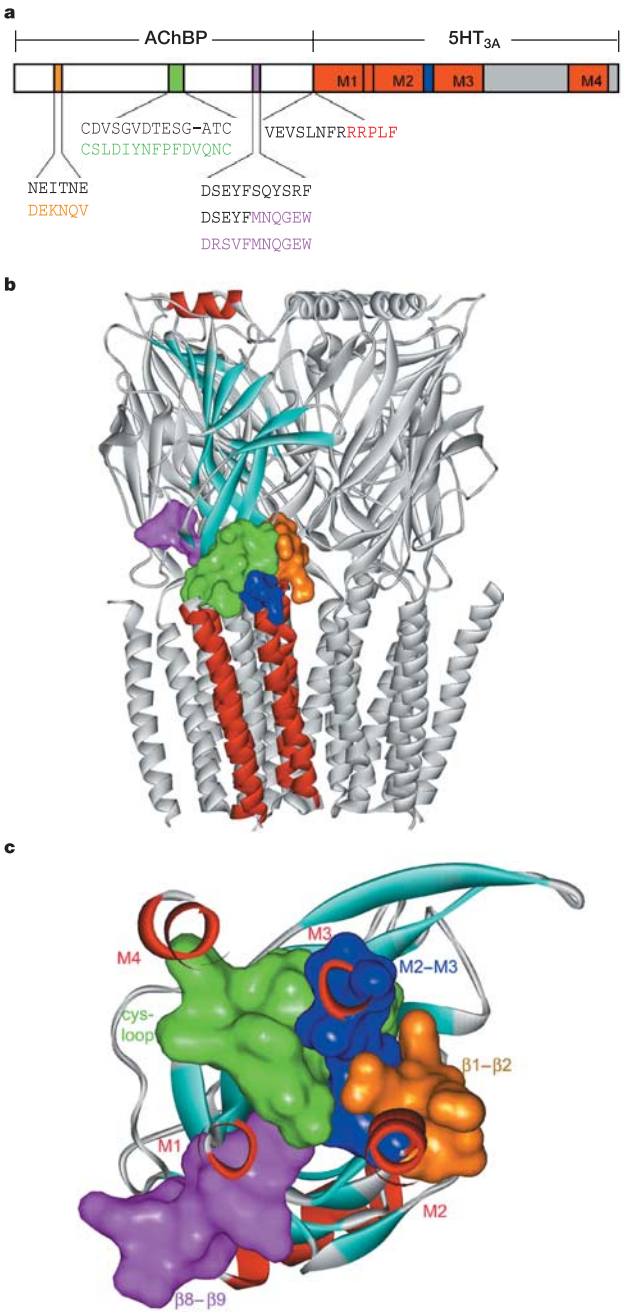

Figure 1 Design and structural model of receptor chimaeras. **a**, Schematic diagram of a subunit composed of AChBP and 5-HT_{3A} sequences. The amino terminus contains AChBP (white bars and black font) and 5-HT_{3A} sequences (loop β1–β2, orange; Cys-loop, green; β8–β9 loop, magenta). The 5-HT_{3A} pore domain follows, with transmembrane helices M1–M4 (red) and the M2–M3 linker (blue). Red font indicates the start of the M1 domain. **b**, Homology model of the chimaeric receptor (C3, Table 1) with key regions of one subunit colour-coded as in **a**. **c**, View of the coupling zone from the pore showing the network of binding and pore domain loops.

Table 1 **Cell surface expression and ACh binding affinity of chimaeric receptors**

Chimaera	$\beta_1\beta_2$	Cys-loop	$\beta_8\beta_9$	Expression (%)	ACh K_d (μM)
AChBP/5-HT_{3A}	AChBP	AChBP	AChBP	100	7.1 ± 2.6 (10)
C1 β1–2	5-HT_{3A}	AChBP	AChBP	120 ± (20 (6)	7.6 ± 0.4 (2)
C1 Cys	AChBP	5-HT_{3A}	AChBP	ND (8)	NM
C1 β8–9	AChBP	AChBP	5-HT_{3A}	6.5 ± 1.5 (4)	NM
C1 β8–9L	AChBP	AChBP	5-HT_{3A} (L)	3.6 ± 1.9 (4)	NM
C2 β1–2, Cys	5-HT_{3A}	5-HT_{3A}	AChBP	ND (8)	NM
C2β1–2, β8–9	5-HT_{3A}	AChBP	5-HT_{3A}	160 ± 14 (4)	15.8 ± 1.5 (1*)
C2 β1–2, β8–9L	5-HT_{3A}	AChBP	5-HT_{3A} (L)	11.0 ± 5.0 (4)	NM
C2 Cys, β8–9	AChBP	5-HT_{3A}	5-HT_{3A}	8.1 ± 1.9 (4)	NM
C2 Cys, β8–9L	AChBP	5-HT_{3A}	5-HT_{3A} (L)	4.5 ± 2.0 (4)	NM
C3	5-HT_{3A}	5-HT_{3A}	5-HT_{3A}	140 ± 26 (6)	155 ± 52 (4)
C3L	5-HT_{3A}	5-HT_{3A}	5-HT_{3A} (L)	190 ± 30 (6)	280 ± 60 (3)
alpha7/5-HT_{3A}	alpha7	alpha7	alpha7	350 ± 32 (4)	138 ± 10 (1*)

C1, C2 or C3 indicate chimaeras with single, double or triple loop substitutions of 5-HT_{3A} sequence. L indicates that β8–β9 linker has three additional residues of 5-HT_{3A} sequence (Fig. 1a). Expression was measured by ^{125}I-α-bungarotoxin binding to intact Bosc 23 cells, and normalized relative to that of the AChBP/5-HT_{3A} chimaera. ACh binding was measured by competition against ^{125}I-α-bungarotoxin binding, yielding the apparent K_d from fitting the Hill equation to the data. Values are means ±s.d. and the number of determinations is in parenthesis. Asterisks indicate where standard error of the fitted parameter is given. ND, not detectable; NM, not measurable owing to low or undetectable expression.

chimaera in which the ligand binding domain of the homomeric alpha7 receptor is joined to the 5-HT_{3A} pore domain (Table 1). On the other hand, when residues in the three loops are substituted in AChBP alone, the resulting soluble protein, C3Ltrunc, shows no change in ACh affinity (AChBP, $K_d = 4.6\,\mu M$; C3Ltrunc, $K_d = 5.8\,\mu M$), showing that residue substitution in the three loops does not directly affect ACh binding, but rather alters affinity by coupling between binding and pore domains. Moreover, ACh evokes inward currents when rapidly applied to cells expressing C3 or C3L, as well as our reference receptor alpha7/5-HT_{3A} (Fig. 2a). Thus low affinity for ACh and functional coupling between binding and pore domains require structural compatibility at the inter-domain interface (Fig. 1c).

To resolve ACh-evoked currents at the level of single channels, we noted that although unitary currents through 5-HT_{3A} receptors are too small to be resolved, this was overcome by neutralizing positively charged residues in the M3–M4 linker on the cytoplasmic face of the membrane[10]. We therefore mutated these arginines to uncharged or negatively charged residues in the chimaeras AChBP/5-HT_{3A}, C3, C3L and alpha7/5-HT_{3A} (see Methods), and looked for ACh-evoked single-channel currents using the cell-attached configuration of the patch clamp. ACh elicits clear-cut single-channel activity in membrane patches from cells expressing conductance-enhanced C3, C3L and alpha7/5-HT_{3A} chimaeras (Fig. 2b); no unitary currents could be detected for the construct derived from AChBP/5-HT_{3A}, despite recording from many patches from cells in which protein expression was confirmed by the presence of green fluorescent protein. Dwell time histograms of the single-channel currents show that the alpha7/5-HT_{3A} and C3 chimaeras open and close with distinct kinetics (Fig. 2c), as might be expected from their different ligand binding domains.

Although the modular composition of our chimaeric receptors accounts for distinct kinetics of pore opening and closing, flow of ions through the pore of each chimaera should be similar[8]. To test this hypothesis, we measured amplitudes of ACh-evoked single-channel currents over a range of membrane potentials. Highly similar slope conductances are observed for conductance-enhanced versions of alpha7/5-HT_{3A}, C3 and C3L, and moderate inward rectification is observed for each, as expected from their common pore domain (Fig. 3).

Our results show functional coupling when amino-acid sequences in all three loops from AChBP are changed to their

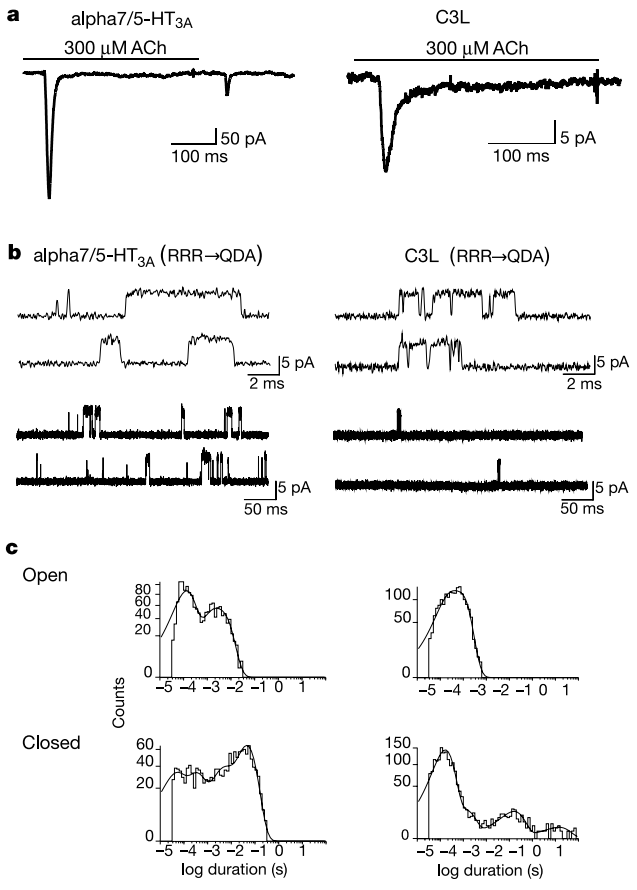

Figure 2 ACh-activated currents through chimaeric receptors. **a**, Whole-cell currents through alpha7/5-HT_{3A} or C3L chimaeras (300 μM ACh). Each trace represents the average of 4 to 8 ACh applications. Decay time constants are 12 ms (alpha7/5-HT_{3A}) and 15 ms (C3L). Holding potential, −50 mV. **b**, Single-channel currents through alpha7/5-HT_{3A} and C3L chimaeras from cell-attached patches (1 mM ACh). Chimaeras contain the triple mutation (RRR → QDA) to increase conductance[10]. Currents are displayed at 9 kHz bandwidth with channel openings as upward deflections. Membrane potential, −70 mV. **c**, Open and closed duration histograms from currents in **b**.

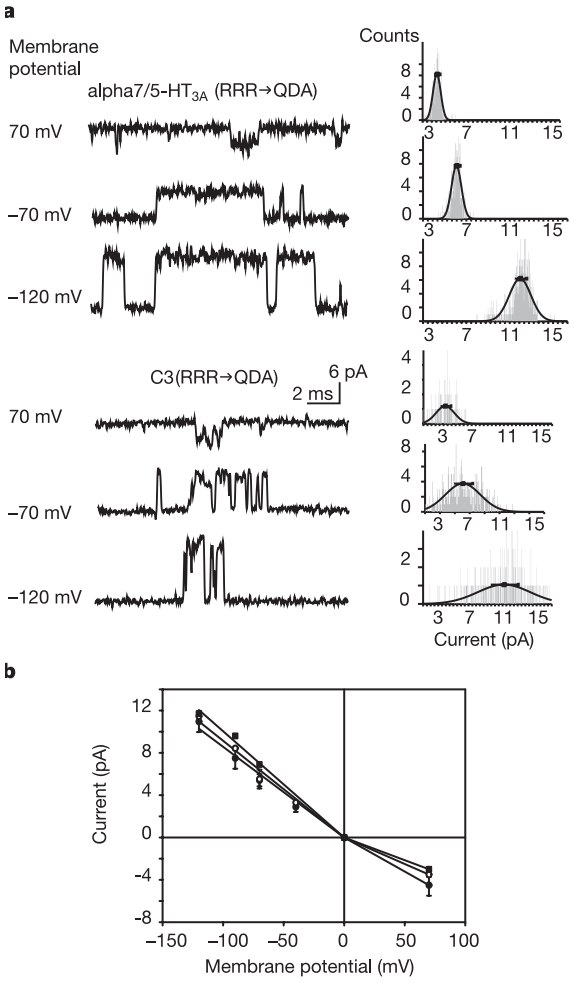

Figure 3 ACh-activated single-channel currents through chimaeric receptors at different membrane potentials. **a**, Unitary currents activated by 1 mM ACh (left) and corresponding amplitude histograms (right) are shown for each chimaeric receptor at the indicated membrane potentials. Bars indicate means ± s.d. **b**, Current–voltage relationships for alpha7/5-HT_{3A} (open circles), C3 (closed circles) and C3L (open squares) containing the triple mutation (RRR → QDA). Each point represents the mean ± s.d. from three different patches. Data were fitted by linear regression. Inward and outward slope conductances are: alpha7/5-HT_{3A} (RRR → QDA), 99 and 57 pS; C3 (RRR → QDA), 91 and 50 pS; and C3L (RRR → QDA), 98 and 43 pS.

5-HT_{3A} counterparts. To determine whether changes in all three loops are required, we generated chimaeras in which only one or two loops in the AChBP module are changed to 5-HT_{3A} sequence, and measured cell surface expression and apparent affinity for ACh (Table 1). Single loop substitutions of either the signature Cys-loop or the β8–β9 linker yielded undetectable or very low expression on the cell surface, suggesting impaired protein folding due to incompatibility within the binding domain or between binding and pore domains. For chimaeras showing undetectable expression on the cell surface, α-bungarotoxin binding to cells made permeable with saponin was also not detectable (data not shown), suggesting impaired folding rather than defective receptor trafficking. Substitution of the β1–β2 linker alone afforded expression of cell-surface receptors similar to AChBP/5-HT_{3A}, but affinity for ACh was unaltered, unlike the functionally coupled C3 and C3L chimaeras, which showed large increases in apparent K_d (Table 1). Conversion of this single-loop chimaera to the conductance-enhanced version, as described for C3 and C3L, afforded robust expression on the cell surface, but no ACh-evoked unitary currents could be detected from cells in which protein expression was confirmed. Four of five of the combinations of double loop substitutions yielded either undetectable or very low expression on the cell surface. The exception to this is the double-loop construct containing 5-HT_{3A} sequences in the β1–β2 and β8–β9 linkers, which shows robust expression. However, this construct shows only a twofold increase in apparent K_d for ACh, distinct from the large increases observed for the functionally coupled C3 and C3L chimaeras (Table 1), and no ACh-evoked single channel currents could be detected from cells expressing the conductance-enhanced version. Thus all three loops from AChBP have to be changed to their 5-HT_{3A} counterparts to produce high expression on the cell surface, low affinity for ACh and functional coupling between binding and pore domains.

The collective findings show a synergistic interplay between three loops from the binding domain and the M2-M3 loop from the pore domain, which is required for efficient expression, shift to low affinity for ACh and opening of the ion pore. Interplay between these loops couples the conformational change at the agonist binding site to the ion pore, and conversely, couples the functional state of the pore to the binding site. Thus the four loops within the coupling zone mediate a bi-directional allosteric interaction between the agonist binding site and distal ion pore.

The chimaeras with compatible inter-domain loops, C3 and C3L, activate in response to ACh and desensitize in its continued presence (Fig. 2), and both active and desensitized states are expected to bind the agonist with high affinity[3]. However, efficient activation requires low affinity of the resting compared with active and desensitized states[11], as well as predominance of the resting state in the absence of ACh. Our steady-state ACh binding measurements reflect the dynamic equilibrium between resting, active and desensitized states. The chimaera with an unmodified AChBP module shows high affinity compared to C3 and C3L chimaeras, but does not show ACh-evoked currents, suggesting its dynamic equilibrium is biased towards the high affinity desensitized state[3]. This bias could arise from significant accumulation of the desensitized state in the absence of ACh, and complete accumulation in its presence. On the other hand, the C3 and C3L chimaeras show low affinity for ACh, suggesting that although they desensitize, their dynamic equilibrium is sufficiently biased towards the low affinity resting state to enable activation by ACh.

Our structural model places the four inter-domain loops proximal to each other, and suggests interactions between particular loops within the subunit as well as between subunits (Fig. 1b, c). Although precise inter-residue contacts require further experimental testing, several general conclusions can be drawn about inter-loop interactions. First, the interplay between binding domain loops occurs through direct or indirect contact among all three loops within the subunit. While the β1–β2 and Cys-loops make direct contact, the β8–β9 loop contacts the Cys-loop indirectly through the intervening strand β10, and projects its side chains into the hydrophobic core of the subunit, impinging upon core side chains from the β1–β2, Cys- and M2–M3 loops (Fig. 1c and Supplementary Information). Furthermore, the β1–β2 loop from each subunit contacts the β8–β9 loop from the adjacent subunit (Fig. 1b). Second, the interplay between loops from the binding and pore domains has striking implications for functional coupling. The binding domain loops β1–β2 and Cys-loop straddle opposite sides of the M2–M3 linker from the pore domain (Fig. 1c), suggesting a twisting motion during coupling that in turn twists the pore-lining M2 domain[12] to allow flow of cations. This twisting motion is probably initiated by motions in parts of the binding domain distal to this region[13], including perturbations due to ACh in the binding pocket and shearing of contacts at subunit interfaces. Additional parts of the pore domain may also contribute to coupling, such as the beginning of the M1 domain, which contacts the Cys-loop. Third, structural compatibility among the four inter-domain loops is likely to be a general requirement for allosteric coupling in rapidly-gated synaptic receptors. Finally, AChBP has the capacity for conformational change upon ACh binding that triggers opening of an ion pore, showing its utility beyond that of a structural surrogate for the ligand binding domain of the Cys-loop receptor superfamily. □

Methods

Construction of chimaeric AChBP/5-HT_{3A} subunits

The cDNA encoding AChBP (ref. 14) was subcloned into the cytomegalovirus-based expression vector pRBG4 (ref. 15), and contained the alpha7 signal sequence[16]. The pore domain from the rat 5-HT_{3A} receptor was joined to AChBP by bridging a *Bsi*WI restriction site at the 3′ end of AChBP and a mutagenically-installed *Kas*I site just 5′ from nucleotides encoding the M1 domain of the rat 5-HT_{3A} receptor, using synthetic double-stranded oligonucleotides[17]. The amino-acid sequence at the M1 junction is shown in Fig. 1a. Conversion of AChBP to 5-HT_{3A} sequence was performed by successive cycles of the QuikChange Site-Directed Mutagenesis kit (Stratagene). To increase unitary conductance for single-channel recordings, we mutated three arginine residues responsible for the low conductance of the 5-HT_{3A} receptors[10] as follows: R432Q, R436D and R440A. All mutant and chimaeric subunits were confirmed by restriction enzyme analysis and sequencing.

Expression of chimaeric receptors

Bosc 23 cells[18] were transfected with the subunit cDNAs using calcium phosphate precipitation, as described previously[17]. A plasmid encoding green fluorescent protein (pGreen lantern) was included to identify transfected cells under fluorescence optics. Cells were studied 2–3 days after transfection.

ACh binding measurements

The number of [^{125}I]α-bungarotoxin sites on the cell surface of transfected cells and ACh competition against the initial rate of [^{125}I]α-bungarotoxin were determined as previously described[19]. ACh binding to water-soluble AChBP and C3Ltrunc was determined as described[16]. Nonspecific binding was determined in the presence of 500 μM D-tubocurarine. The Hill equation was fitted to the competition measurements to yield the apparent dissociation constant, K_d and the Hill coefficient. To measure binding of α-bungarotoxin to intracellular complexes, cells were first made permeable with 0.5% saponin (w/v) (ref. 20).

Single-channel recording

Recordings were obtained in the cell-attached configuration at 20 °C. Extracellular and pipette solutions contained 142 mM KCl, 5.4 mM NaCl, 0.2 mM $CaCl_2$ and 10 mM HEPES (pH 7.4). Single-channel currents were recorded using an Axopatch 200B patch-clamp amplifier (Axon Instruments, Inc.), digitized at 5 μs intervals with the PCI-6111E interface (National Instruments), recorded to hard disc using the program Acquire (Bruxton Corporation) and detected by the half-amplitude threshold criterion using the program TAC (Bruxton Corporation) at a final bandwidth of 10 kHz (ref. 21). Open and closed time histograms were plotted using a logarithmic abscissa and a square-root ordinate[22] and fitted to the sum of exponentials by maximum likelihood.

Macroscopic current recording

Macroscopic currents were recorded in the whole-cell configuration[23] using a perfusion system that allowed rapid (0.1–1 ms) solution exchange[24,25]. The pipette solution contained 140 mM KCl, 5 mM EGTA, 5 mM $MgCl_2$ and 10 mM HEPES, pH 7.3. Extracellular solution contained 150 mM NaCl, 5.6 mM KCl, 0.2 mM $CaCl_2$ and 10 mM HEPES, pH 7.4. A series of 200–400 ms applications of ACh was applied to each cell. Macroscopic currents were filtered at 5 kHz, digitized at 20 kHz and analysed using IgorPro software (WaveMetrics Inc.). The following exponential function was fitted to

average currents from four to eight ACh applications: $I_{(t)} = I_0 \exp(-t/\tau_d) + I_\infty$ where I_0 and I_∞ are the peak and the steady state currents, respectively, and τ_d is the time constant of current decay.

Homology modelling

A homology model of our receptor chimaera (Fig. 1b, c) was generated using version 6.0 of the program MODELER[26], together with spatial restraints provided by AChBP[1] and *Torpedo* acetylcholine receptor pore domain[2] structures, as described[27]. Briefly, we aligned by homology the sequence of the chimaera C3 (Fig. 1a) with that of AChBP fused to the pore domain of the *Torpedo* receptor; the A subunit from AChBP was joined to the pore domain of the alpha$_1$ subunit, B to gamma, C to alpha$_2$, D to delta and E to beta. To maintain complementarity between subunits at their interfaces, all five subunits were modelled simultaneously. We used the 'patch' command in MODELER to constrain coordinates of cystines 128 and 142, which form a disulphide bond in each subunit. Among several options in MODELER, we selected the 'refine1 mode', which generates the highest level of refinement using conjugate gradients coupled with simulated annealing and molecular dynamics. Modelling included all polar hydrogens to allow for main chain hydrogen bonding, but omitted non-polar hydrogens.

Received 17 May; accepted 14 June 2004; doi:10.1038/nature02753.

1. Brejc, K. *et al.* Crystal structure of an ACh-binding protein reveals the ligand-binding domain of nicotinic receptors. *Nature* **411,** 269–276 (2001).
2. Miyazawa, A., Fujiyoshi, Y. & Unwin, N. Structure and gating mechanism of the acetylcholine receptor pore. *Nature* **423,** 949–955 (2003).
3. Sine, S. M. The nicotinic receptor ligand binding domain. *J. Neurobiol.* **3,** 431–446 (2002).
4. Karlin, A. Emerging structure of the nicotinic acetylcholine receptors. *Nature Rev. Neurosci.* **3,** 102–114 (2002).
5. Changeux, J. P. & Edelstein, S. J. Allosteric receptors after 30 years. *Neuron* **21,** 959–980 (1998).
6. Grosman, C., Salamone, F., Sine, S. M. & Auerbach, A. The extracellular linker of muscle acetylcholine receptors is a gating control element. *J. Gen. Physiol.* **116,** 327–339 (2000).
7. Kash, T., Jenkins, A., Kelly, J., Trudell, J. & Harrison, N. L. Coupling of agonist binding to channel gating in the GABA$_A$ receptor. *Nature* **421,** 272–275 (2003).
8. Eisele, J. L. *et al.* Chimaeric nicotinic-serotonergic receptor combines distinct ligand binding and channel specificities. *Nature* **366,** 479–483 (1993).
9. Quiram, P. & Sine, S. M. Identification of residues in the neuronal α7 receptor that confer selectivity for conotoxin ImI. *J. Biol. Chem.* **273,** 11001–11006 (1998).
10. Kelley, S., Dunlop, J., Kirkness, E., Lambert, J. & Peters, J. A. A cytoplasmic region determines single-channel conductance in 5-HT$_3$ receptors. *Nature* **424,** 321–324 (2003).
11. Jackson, M. B. Perfection of a synaptic receptor: kinetics and energetics of the acetylcholine receptor. *Proc. Natl Acad. Sci. USA* **86,** 2199–2203 (1989).
12. Unwin, N. Acetylcholine receptor channel imaged in the open state. *Nature* **373,** 37–43 (1995).
13. Unwin, N., Miyazawa, A., Li, J. & Fujiyoshi, Y. Activation of nicotinic acetylcholine receptor involves a switch in conformation of the alpha subunits. *J. Mol. Biol.* **319,** 1165–1176 (2002).
14. Hansen, S. B. *et al.* Tryptophan fluorescence reveals conformational changes in the acetylcholine binding protein. *J. Biol. Chem.* **277,** 41299–41302 (2002).
15. Lee, B. S., Gunn, R. B. & Kopito, R. R. Functional differences among nonerythroid anion exchangers expressed in a transfected human cell line. *J. Biol. Chem.* **266,** 11448–11454 (1991).
16. Gao, F. *et al.* Curariform antagonists bind in different orientations to acetylcholine binding protein. *J. Biol. Chem.* **278,** 23020–23026 (2003).
17. Sine, S. M. Molecular dissection of subunit interfaces in the acetylcholine receptor: identification of residues that determine curare selectivity. *Proc. Natl Acad. Sci. USA* **90,** 9436–9440 (1993).
18. Pear, W. S., Nolan, G. P., Scott, M. L. & Baltimore, D. Production of high titer helper-free retroviruses by transient transfection. *Proc. Natl Acad. Sci. USA* **90,** 8392–8396 (1993).
19. Sine, S. M. & Taylor, P. Functional consequences of agonist-mediated state transitions in the cholinergic receptor. *J. Biol. Chem.* **254,** 3315–3325 (1979).
20. Prince, R. J. & Sine, S. M. Molecular dissection of subunit interfaces in the acetylcholine receptor: identification of residues that determine agonist selectivity. *J. Biol. Chem.* **271,** 25770–25777 (1996).
21. Wang, H.-L. *et al.* Acetylcholine receptor M3 domain: stereochemical and volume contributions to channel gating. *Nature Neurosci.* **2,** 226–233 (1999).
22. Sigworth, F. & Sine, S. M. Data transformations for improved display and fitting of single-channel dwell time histograms. *Biophys. J.* **52,** 1047–1054 (1987).
23. Hamill, O. P., Marty, A., Neher, E., Sakmann, B. & Sigworth, F. J. Improved patch-clamp techniques for high-resolution current recording from cells and cell-free membrane patches. *Pflugers Arch.* **391,** 85–100 (1981).
24. Liu, Y. & Dilger, J. P. Opening rate of acetylcholine receptor channels. *Biophys. J.* **60,** 424–432 (1991).
25. Spitzmaul, G., Dilger, J. P. & Bouzat, C. The noncompetitive inhibitor quinacrine modifies the desensitization kinetics of muscle acetylcholine receptors. *Mol. Pharmacol.* **60,** 235–243 (2001).
26. Sali, A. & Blundell, T. L. Comparative protein modelling by satisfaction of spatial restraints. *J. Mol. Biol.* **234,** 779–815 (1993).
27. Sine, S. M., Wang, H.-L. & Bren, N. Lysine scanning mutagenesis delineates structural model of the nicotinic receptor ligand binding domain. *J. Biol. Chem.* **277,** 29210–29223 (2002).

Supplementary Information accompanies the paper on **www.nature.com/nature**.

Acknowledgements This work was supported by grants from the National Institutes of Health, UNS, ANPCyT and F. Antorchas, Argentina.

Competing interests statement The authors declare that they have no competing financial interests.

Correspondence and requests for materials should be addressed to S. M. S. (sine@mayo.edu).

Identification of an antimalarial synthetic trioxolane drug development candidate

Jonathan L. Vennerstrom[1], Sarah Arbe-Barnes[2], Reto Brun[3], Susan A. Charman[4], Francis C. K. Chiu[4], Jacques Chollet[3], Yuxiang Dong[1], Arnulf Dorn[5], Daniel Hunziker[5], Hugues Matile[5], Kylie McIntosh[4], Maniyan Padmanilayam[1], Josefina Santo Tomas[3], Christian Scheurer[3], Bernard Scorneaux[3], Yuanqing Tang[1], Heinrich Urwyler[6], Sergio Wittlin[3] & William N. Charman[4]

[1]*College of Pharmacy, University of Nebraska Medical Center, 986025 Nebraska Medical Center, Omaha, Nebraska 68198-6025, USA*
[2]*Fulcrum Pharma Developments Ltd, Hemel Hempstead, Hertfordshire HP1 1JY, UK*
[3]*Swiss Tropical Institute, Socinstrasse 57, CH-4002 Basel, Switzerland*
[4]*Victorian College of Pharmacy, Monash University, 381 Royal Parade, Parkville, Victoria 3052, Australia*
[5]*F. Hoffmann-La Roche Ltd, Grenzacherstrasse 124, CH-4070 Basel, Switzerland*
[6]*Basilea Pharmaceutica Ltd, Grenzacherstrasse 487, CH-4058 Basel, Switzerland*

The discovery of artemisinin more than 30 years ago provided a completely new antimalarial structural prototype; that is, a molecule with a pharmacophoric peroxide bond in a unique 1,2,4-trioxane heterocycle[1]. Available evidence[2–4] suggests that artemisinin and related peroxidic antimalarial drugs exert their parasiticidal activity subsequent to reductive activation by haem, released as a result of haemoglobin digestion by the malaria-causing parasite. This irreversible redox reaction produces carbon-centred free radicals, leading to alkylation of haem[5] and proteins (enzymes)[6], one of which—the sarcoplasmic-endoplasmic reticulum ATPase PfATP6 (ref. 7)—may be critical to parasite survival. Notably, there is no evidence of drug resistance to any member of the artemisinin family of drugs[8]. The chemotherapy of malaria has benefited greatly from the semi-synthetic artemisinins artemether and artesunate as they rapidly reduce parasite burden, have good therapeutic indices and provide for successful treatment outcomes[9]. However, as a drug class, the artemisinins suffer from chemical[10] (semi-synthetic availability, purity and cost), biopharmaceutical[11] (poor bioavailability and limiting pharmacokinetics) and treatment[8,11] (non-compliance with long treatment regimens and recrudescence) issues that limit their therapeutic potential. Here we describe how a synthetic peroxide antimalarial drug development candidate was identified in a collaborative drug discovery project.

The drug discovery process relied on prospective multidimensional lead optimization made possible by rapid and iterative integration of antimalarial, physicochemical, metabolism, pharmacokinetic and toxicity data that guided the medicinal chemistry. In comparison to the semi-synthetic artemisinins (Fig. 1a), the selected 1,2,4-trioxolane drug development candidate (trioxolane **7**; also known as OZ277 or RBx-11160, Fig. 1e) exhibits structural simplicity, an economically feasible and scalable synthesis, superior antimalarial activity and an improved biopharmaceutical profile. It has progressed through formal pre-clinical regulatory studies, and will be advanced into 'first-in-man' clinical studies during 2004.

The essential characteristics for a new trioxolane antimalarial drug product were identified early in the discovery process to guide compound progression, and they ultimately led to selection of a development candidate. Key features included low product costs requiring a straightforward synthesis and simple formulation approaches, a maximum 3-day treatment regimen with once-daily administration necessitating good potency and pharmacokinetic